Journal of Power Sources 194 (2009) 408–422

Contents lists available at ScienceDirect

Journal of Power Sources

journal homepage: www.elsevier.com/locate/jpowsour

Microstructural characterization of solid oxide fuel cell electrodes by image analysis technique

Andrea Lanzini*, Pierluigi Leone, Pietro Asinari

Dipartimento di Energetica - Politecnico di Torino, Corso Duca degli Abruzzi 24, 10129 Torino, Italy

ARTICLE INFO

Article history:
Received 10 July 2008
Received in revised form 19 April 2009
Accepted 26 April 2009
Available online 3 May 2009

Keywords:
Image analysis
3D electrode reconstruction
SOFC
Micro-modelling
Electrode design
Nickel coarsening

ABSTRACT

The paper deals with the microstructural characterization of electrodes of solid oxide fuel cells based on processing of 2D images. The interest relies on finding the reliable description of the structures which determine the microscopic image, by means of parameters involving the morphology, the shape and the size of elementary structures, and the microscopic topology in terms of spatial connectivity functions. The use of detailed mathematical methods allowed one to reconstruct the 3D structure of both fuel and air electrodes having 2D images as input.

The analysis was applied to an anode-supported cell with NiO based anode, 8YSZ electrolyte and LSM/YSZ cathode. The microscopic analysis was performed by means of both a SEM and an optical microscope before and after the electrical testing of the cell.

The obtained images were processed and a quantitative analysis was performed for achieving information concerning the microstructure and including: phases' fraction, grain size, granulometry law, constituent shape factors, phase spatial organization and descriptive functions. The microstructure features were analyzed by means of one-point and two-point statistics. It was possible to build 3D structures of the electrodes: anode and the double-layer cathode.

The work also points out some issues related to the proper use of the observed microscopic parameters and topology functions as inputs for electrodes' modelling. In the work, the results of the image analysis are used with a simple analytical model with the aim to estimate the optimal design of the cathode current functional layer (CFL). It is proved that the actual cell design with 15 μm thick CFL was optimized for a temperature as high as 850 °C, with a charge transfer and total ohmic resistance of around 0.2 Ω cm^2. More generally, results of image analysis can be used efficiently as input in the multi-scale modelling of SOFC electrodes considering macroscopic and mesoscopic models.

1. Introduction

1.1. General considerations

Solid oxide fuel cells are considered a promising technology matching the energy vision of tomorrow, that is high efficiency, low emissions, multi-fuel capability. Several issues are under investigations and concern the use of low-cost and effective manufacturing procedures, the increase of cell power density with the reduction of the operating temperature, the understanding and limitation of degradation phenomena related to its long-term operation. In this scenario, the reliable microscopic analysis of the cells is of very importance and it has high relevance. The capability of analyze microscopic features is a key discriminator for design of high performance and robust fuel cells. The evaluation of location of reaction sites in the electrodes, the charge transport properties of manufactured layers, the micro-fluidic properties of reactive species and the evolution of microstructure due to degradation phenomena are only possible coupling high quality microstructural analysis and modelling.

This paper deals with an experimental analysis of SOFC ceramic planar cells in order to analyze and evaluate their design, with some further considerations regarding the degradation processes. A reliable description of the microstructures of the electrodes was conducted by means of parameters involving the morphology, the shape and the size of elementary structures, and the microscopic topology in terms of spatial connectivity functions.

1.2. Overview of image analysis techniques

Advanced techniques for cell characterization are recently indicated as prior to enhance the quality of research in fuel cells and

* Corresponding author. Tel.: +39 320 9323520; fax: +39 011 0904523.
E-mail address: andrea.lanzini@polito.it (A. Lanzini).

0378-7753/$ – see front matter © 2009 Elsevier B.V. All rights reserved.
doi:10.1016/j.jpowsour.2009.04.062

push the technology into levels for market penetration. Advanced methods include the possibility to characterize microscopic features, mechanical properties and thermal properties of cells, often in relation to steady state or transient operating conditions [1–5].

In particular images analysis techniques and structures reconstruction methods have been proposed as powerful and reliable tools in the fuel cell research. Studies by scanning electron microscopy (SEM) are limited to scales of micron and submicron. Transmission electron microscope (TEM) is the preferred analytical technique on a nanoscale level but traditionally, the use of TEM for interface study in SOFC was rather limited due to the difficulties in specimen preparation [6]. Recently, Focused Ion Beam (FIB) technique has become an effective method for TEM specimen preparation. FIB TEM enables 3D analysis of electrode microstructure in terms of particle and pore size distribution, triple-phase boundary density and pore tortuosity [3,4]. However, image analysis techniques applied to SOFCs have been investigated since few years ago also using classical approaches. These methods remain nowadays the most popular because of the low cost of equipments and the instrumentation, which has already large-diffusion. Image analysis techniques have been proposed by Simwonis et al. [7] to evaluate degradation of Ni/YSZ anodes in SOFCs. Ni-granulometry curves of operated cells after different operational times were reported. Lee et al. investigate the microstructure of a Ni cermet anode generating elemental maps of the main solid species and pores [8] and afterwards they use some of those information in order to estimate the electrical properties of electrodes using electrochemical methods [9,10]. In [11] 3D structural reconstructions of fuel cell electrodes were achieved using methods based on one-point statistics or the granulometry law and two-point statistics. The latter provides a more reliable reconstruction since it takes into account both porosity and the two-point autocorrelation function, which provides information about the connectivity of the pores in the porous medium. The reconstructed topologies of PEM and SOFC electrodes were then analyzed in terms of their micro-fluidic properties. Image analysis is also used to evaluate degradation phenomena and the evolution of the microstructures during steady state [7] and transient operation [5]. 3D structure reconstructions were also achieved using an experimentally based approach with FIB technique coupled with TEM analysis [3].

Information obtained from image analysis can be used in modelling, including cell performance and degradation phenomena. Many research focused on micro-modelling of fuel cells [12–21], results leaded to encouraging indications and conclusions about cell optimization. An optimized microstructure of a SOFC electrode should have (1) long-range connectivity of respective ionic and electronic conductor chains stretching across the electrode and linking the current collector to the electrolyte; (2) maximized active sites of three-phase boundary (TPB) for electrochemical reactions. These requirements warrant an optimal ratio of ionic to electronic conductors, in terms of their volume and average grain size, in a properly sintered electrode. In addition to the required microstructure for enhancing conversion of ionic to electronic current taking place at the TPB and transport of these currents along their respective "active bond" (chains), there is other important consideration such as efficient gas diffusion from the bulk into the reaction sites.

The charge transport properties were well identified and discussed in [16–19,21] and some experimental results on commercial cells confirmed the results achievements of that analysis [19]. Mass transport phenomena in a solid phase of SOFC electrodes were detailed faced by Asinari et al. [22].

1.3. Overview of the work of this paper

In this paper, digital images related to electrodes' microstructures were obtained from different techniques (SEM, energy dispersive spectrometer—EDS, optical microscope). The images were then processed and a quantitative analysis was performed achieving information concerning the microstructure and including: phases' fraction, grain size, granulometry law, constituent shape factors, phase spatial organization and descriptive functions. The microstructure features were analyzed by means of one-point and two-point statistics. It was possible to build 3D structures of the main cell's layers using Truncated-Gaussian methods [23].

An image analysis procedure has been developed to determine the main morphological and geometrical properties of the investigated cell. Once collected SEM and optical images, they have been analyzed through an in-house developed code and new software called CHIMERA® [24]. Contrast enhancing and noise filtering plus others common image adjusting settings has been used to eliminate defects in the acquired images. Regarding the porous electrodes, the adjusted images have been then bounded to distinguish the porous phase from the solid phase (binary thresholding). With some images, it has been also possible to distinguish the different solid phases of the electrode: the electronic phase (Ni for the anode, and LSM for the cathode) and ionic phase (8YSZ for both electrodes). This allowed us to perform a micro-modelling of the composite electrodes to estimate their electrical and electrochemical performances.

The analysis was applied to brand new cells and tested cells pointing out degradation phenomena such as the nickel agglomeration; in particular, we made a detailed analysis of the microscopic features of SOFC layers including anodes and double-layer cathodes pointing out to the cathode design and the anode microstructure degradation.

The information obtained by the image analysis was also used combined with analytical models in order to estimate the design properties of the layers. We focused our work on some models presented in the previously discussed works, in particular on the charge transfer model and the percolation theory, since they showed good agreement with experimental data. We modelled every cell's layer, with particular attention to the cathode functional layer, since it is expected to be a major source of losses in the cell. Our main objective was to determine if such commonly used models, that describe the electrical and electrochemical properties of SOFC composite electrodes (such as LSM/8YSZ for cathode, and Ni/8YSZ for anode) are good to predict the optimum design configuration, which essentially means the proper designing of electrodes porosity, grain size of particles, volume fraction of the ionic and the electronic phases, thickness of active layers and current-collecting layers, etc. The work also points out some issues related to the reliable use of the observed microscopic parameters as inputs for those models. To perform this effectively, we considered a commercial SOFC planar cell (ASC1 cell), which deploys composite electrodes and whose design is later described. We referred to our previous work [25], where some electrical and electrochemical macroscopic parameters were extrapolated through parameter estimation form experimental polarization curves. Concerning the estimated parameters, we used the estimation of the $i_{0,cat}$ (equilibrium exchange current density) as an input to define the charge transfer resistance, $R_{ct,eff}$, of the cathode functional layer (which is used in model of effective charge transfer by Tanner et al. [12,13]). Then, we coupled microscopic observations of the cell's electrodes, obtained through image analysis techniques, and the calculated $R_{ct,eff}$ was employed to evaluate the actual design of the ASC1 active cathode in terms of geometrical and microstructural parameters. It was concluded that the present design of the cell is optimized for operating at a temperature as high as 850 °C. A thicker electrode would be required for minimizing losses at lower temperature. Moreover, results of image analysis can be used as input in multi-scale modelling approaches from analytical to complex mesoscopic models of SOFC electrodes [22].

2. Experimental

2.1. Experimental setup: polarization analysis

The tests were performed with circular shaped anode-supported SOFC cells with a diameter of 80 mm and an active area of 47 cm^2. The actual macroscopic geometrical features were determined from SEM of the cells. The geometry and materials of the cell were:

- ASC1: anode 525–610 μm thick with two layers (both made of NiO/8YSZ cermet: functional layer 5–10 μm thick; support layer 520–600 μm thick); electrolyte 4–6 μm thick $Y_{0.16}Zr_{0.84}O_2$ (8YSZ), with unknown volume density; cathode 30–40 μm thick with two layers (functional layer of porous 8YSZ and $La_{0.75}Sr_{0.2}MnO_3$ (LSM); current-collecting layer of LSM alone).

The cell run around 200 h with 0.5 l min^{-1} of hydrogen humidified at 30 °C and 1.5 l min^{-1} of air at the cathode side. The cell was tested in the range between 650 °C and 850 °C taking several polarization curves and in generally operating at relative low current load (0.3 A cm^{-2}) and fuel utilization factors higher than 40%. Further details about the test-rig have been presented in [25].

2.2. Experimental setup: microscopy analysis

The information about the microstructural properties of the ASC1 cell was obtained from both a scanning electron microscope (SEM) ZEISS EVO 40 and an optical microscope LEICA REICHERT MeFe3.

We focused our analysis on the same type of cell (ASC1), viewed firstly as brand new and subsequently after that complete polarization test session was performed. The reason for this was not only to evaluate degradation phenomena occurring on an anode-supported cell, but also to evaluate the microstructural characteristics of the cell under operating conditions after the NiO is reduced to metallic Ni. The reduction step occurs when hydrogen is flowed to cell and could be considered in same way as the last step of the manufacturing of a cell. The microstructural change of a cell after anode reduction is quite significant. In [26] Haanappel and Smith have studied the effect of the reduction temperature on the subsequent cell electrochemical behaviour, seeing that at higher temperature of reduction the cell performances improve. In a previous work [27], we demonstrated that after the reduction step, the Young modulus of an anode-supported planar SOFC decreased from 108 to 50 GPa.

Our cell has been reduced at a temperature of 800 °C. During the heating-up phase the anode side is fed by 500 ml min^{-1} flow of N_2/H_2 mixture (95/5 vol.%) after the set-point temperature is reached, the nitrogen flow is gradually substituted by hydrogen.

3. Methodology of microscopic analysis

After collecting a set of images for the whole cell and each of its functional layers, the average thickness of each layer has been evaluated. Subsequently, for the composite electrodes (anode substrate and functional cathode) we evaluated porosity, volume fraction and distribution of solid and pore phases along with their mean grain sizes. These morphological properties have been estimated by means of software CHIMERA®. This software has been developed essentially to be helpful for oil companies in the recovery efforts of oil and gas from underground and undersea reservoirs. It allows one to analyze images of porous and/or composite media, to distinct each phase present in it, and eventually reconstruct a 3D model structure from 2D image samples in order to evaluate important properties such as permeability of the fluid phase and capillarity pressure in the fluid channels. We found out that the tools of CHIMERA® could be useful as well for the field of fuel cells and their microstructural and morphological characterization. A more detailed description on how this software works and how we used it for our purposes is reported in the next section.

In Table 1, the main steps of the image analysis procedure adopted in this work are summarized.

3.1. Microscopic properties of ASC1 electrodes

As said before, we performed the image analysis procedure through the software CHIMERA®. The strong features of this software, compared to other available commercial software such as

Table 1
Steps for image analysis.

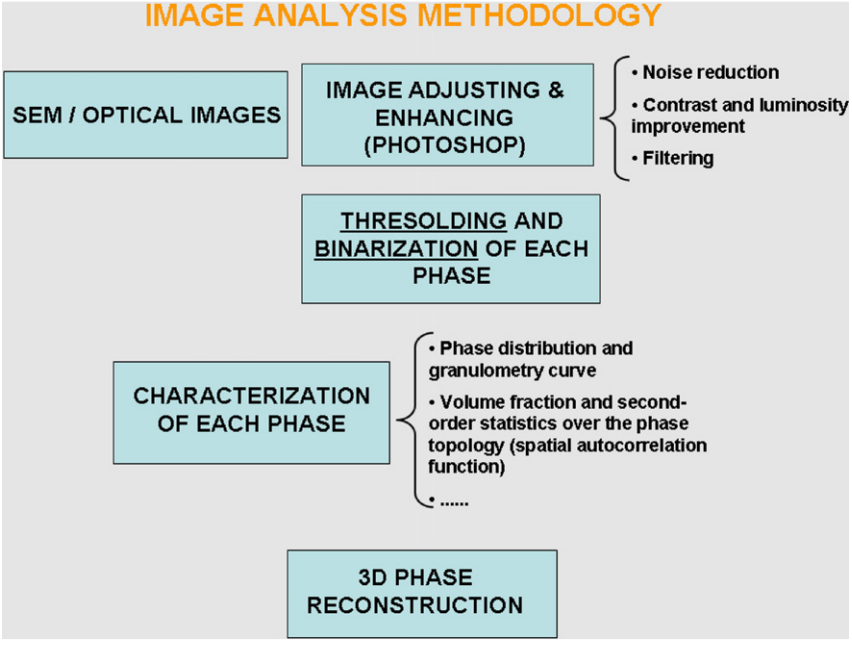

FOVEA PRO® (a plug-in tool-box of ADOBE PHOTOSHOP®) are (i) several binarization methods to extrapolate each phase from a composite structure in order to improve accuracy and compare uncertainties related with each method; (ii) deeper mathematical methods used to analyse the distribution of each phase and to reconstruct the 3D structure having 2D binary images as input; (iii) easy tool to average granulometry distribution curves and manage also large set of images. In Section 3.2 we illustrate in a synthetic way the methodology we followed to analyze SEM and optical images of new and operated ASC1 cells.

3.2. Image analysis for a Ni/8YSZ anode support

This section reports the procedure presented above, and deployed in this paper to analyze the anode support structure of an ASC1 cell. The same procedure has been used for all the images characterized in this paper.

The first step has been to collect several back-scattered SEM images of grinded and polished sections of a brand new ASC1 cell. The back-scattering electrons detector allows one to see each material in different color intensity over a gray-scale tone depending on the atomic number of the material from which the electron is scattered. For a composite structure such as that of a Ni/8YSZ anode, this microscopic imaging technique is then really helpful to distinguish each phase from another. For example, in the anode structure three different phases can be distinguished, two solids, the NiO or Ni-phase (depending on whether the reduction step has already occurred or not) and the 8YSZ phase, and one void, due to the pores of the electrode. The resolution for this set of SEM images, with a magnitude of 1000×, is 3.6 pixels μm^{-1}; this value is obtained directly from the micron bars shown on each image.

We took into consideration five images of the anode support section in order to evaluate average properties of this component. This is certainly not a statistically meaningful set, and a more proper way to handle this would be to develop a software tool which extracts hundreds of sub-pictures from the experimental ones and then it repeats the following procedure. This is what we are planning to do in our future works on image analysis.

The selected images have then been adjusted and filtered from noise and other disturbs through the commercial software. This is similar to what done by Lee et al. in their work on image analysis [8,9]. The scope is being able to well distinguish each phase of the composite electrode before the binarization step.

The second step is to isolate each phase trough the thresholding procedure. From the gray histogram of the selected image we decide where to truncate the gray curve determining which pixels belong to a certain phase and which not. The output consists of three binarized images; each one representing just the pixels in a certain gray interval for that particular phase, that namely are the “Pores” phase, the “Ni” phase and the “Zr” phase (this last label refers to the YSZ phase).

This procedure is somewhat an arbitrary method, which makes all the image analysis procedure somewhat arbitrary. However this is unavoidable, because in order to separate each phase from another, it is necessary to define some threshold levels in the gray-scale, which allow one to consider all the pixels, ranging in a certain gray-scale interval, belonging to a univocal phase. Since each image always differs from the others (for example in terms of contrast, luminosity and other parameters), the thresholding process is neither simple nor an automatic step. However, high quality images usually reduce the sensitivity of the obtained post-processing results from the adopted thresholds.

In Fig. 1, it is shown a composite anode’s SEM image taken under consideration for this work. As said before, the images have been taken in back-scattering in order to better discriminate not only

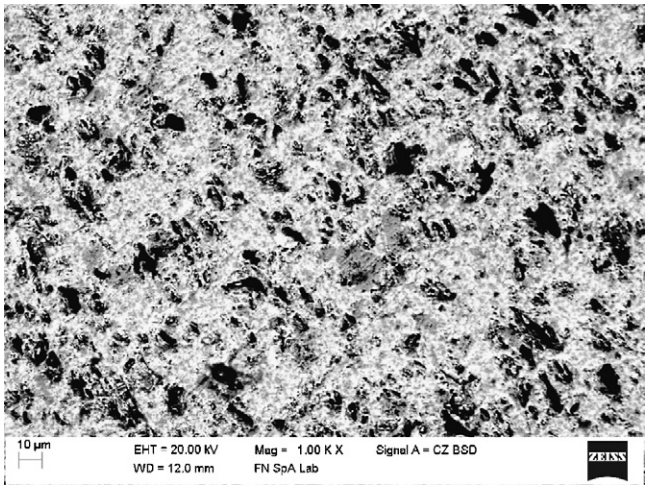

Fig. 1. SEM image of ASC1 anode support after the step of image adjusting and contrast enhancing.

the pores phase form the solid ones, but also to distinguish ion and electron conducting materials. It is possible to distinguish the solid phase due to Ni from that one due to Zr. Since the Ni has a higher atomic number, the Ni-phase is the gray one, besides the white one is attributed to the Zr-phase.

In Fig. 2, it is shown how the pores phase of the anode region represented in Fig. 1 has been separated from the others phase. This is the so-called binarization step and it can be easily performed by commercial software for image analysis. Since they generally make possible only to separate each phase at once, for this procedure we developed a homemade simple code that starting from an SEM-BSE image, ascribe the original image pixels to a specific phase and then shows maps of each phase, accounting for the number of pixels belonging to it. The threshold levels have been user-defined taking into account the image histogram shaping. The output of the binarized phases is then showed in Fig. 3.

The same work has been performed by using the EDS element mapping with the OXFORD Instruments® microanalysis equipment installed on the SEM microscope used for this work. The region scanned with EDS is reported below, in Fig. 4. The output mapped image is shown in Fig. 5. The aim was to perform the binarization of each phase using as source an image where Ni- and YSZ phase were both distinguishable through a techniques other than back-scattering. Through EDS mapping with green color the Ni element is mapped, and with red color the Zr element. We actually succeed very well in this operation, as shown in Fig. 6, where we selected

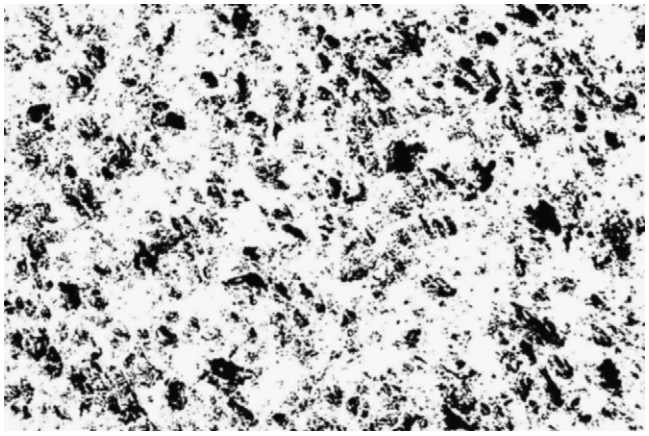

Fig. 2. Binary image of the pores phase of image of Fig. 1.

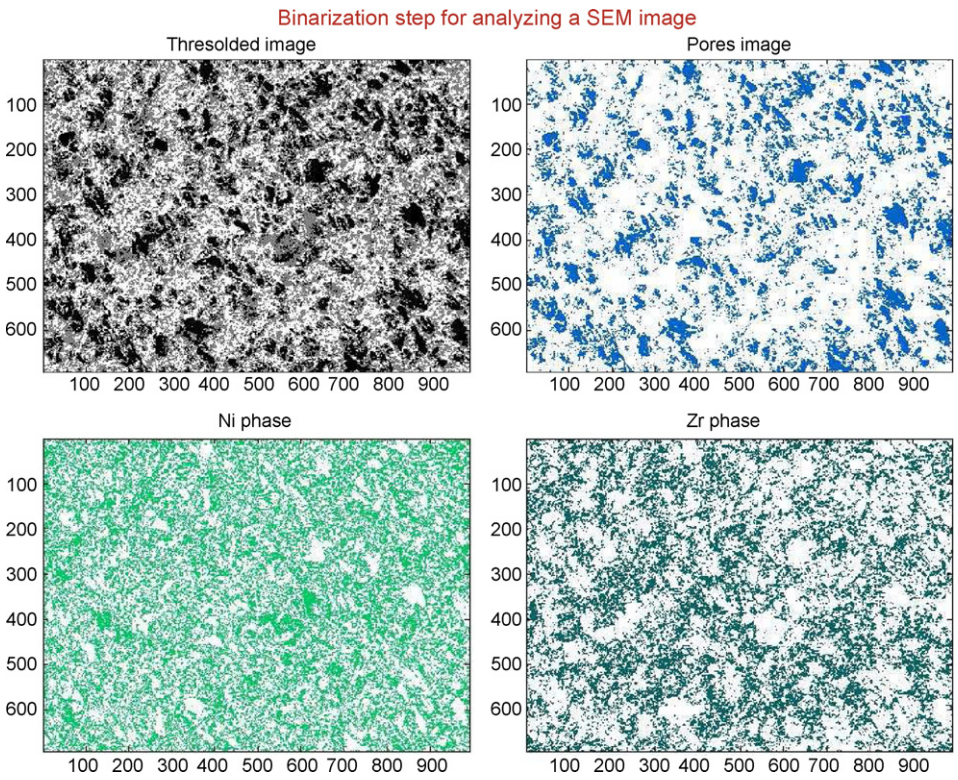

Fig. 3. Binarized images of each phase present in Fig. 1.

a small region of the precedent image (Fig. 5); it is clearly visible a very large agglomerate of Ni.

The purpose was to show that EDS mapping can be an alternative technique to acquire images of composite electrodes in order to have ionic phase well-distinguishable from the electronic phase. Also optical images confirmed the validity of our preceding statement by EDS analysis. However, EDS mapping takes longer to be performed and is not straight-forward to set appropriately the microscope parameters in order to acquire good and reliable maps. For these reasons, in this work, we used essentially BSE images for image analysis.

At the top of the SEM image in Fig. 4, are visible the cathodic double layer, and the thin 8YSZ electrolyte; the rest of the image is the anode support. The biggest black holes are large pores that could represent residual air bubble in the tape-casted anode slurry. Apart from them, the porosity appears homogeneously distributed and has been estimated by image thresholding as 26%.

In what following, the procedure for the characterization of a single binarized phase, e.g. the pore phase, is described. The analysis presented below has been repeated exactly the same manner for the two other phases present in anode (namely the YSZ phase and the Ni-phase).

As said before, we took into account five SEM-BSE pictures at 1000×, representing different region of anode support of ASC1. Each sample refers to a random physical portion of electrode considered for the analysis.

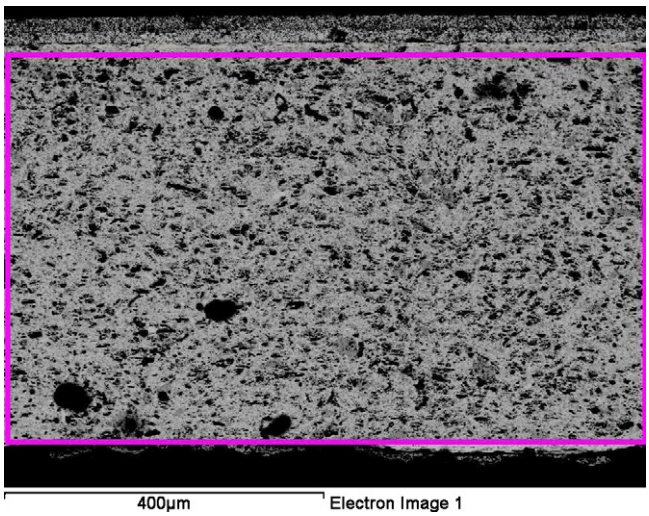

Fig. 4. SEM-BSE image of whole cell section.

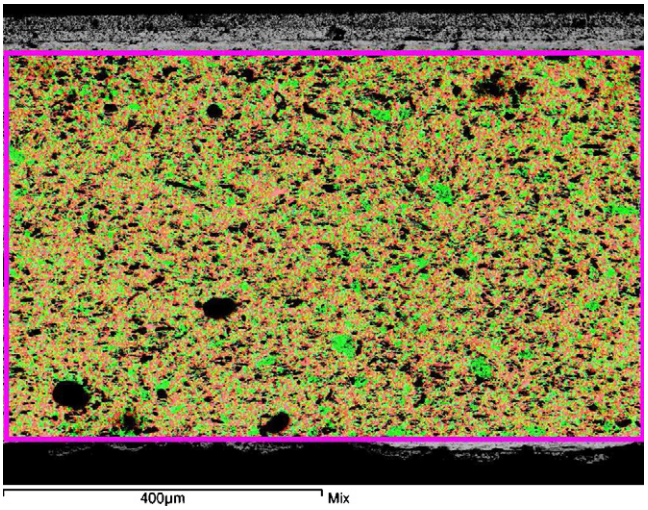

Fig. 5. EDS mapping of Ni (green) and Zr (red). (For interpretation of the references to color in this figure legend, the reader is referred to the web version of the article.)

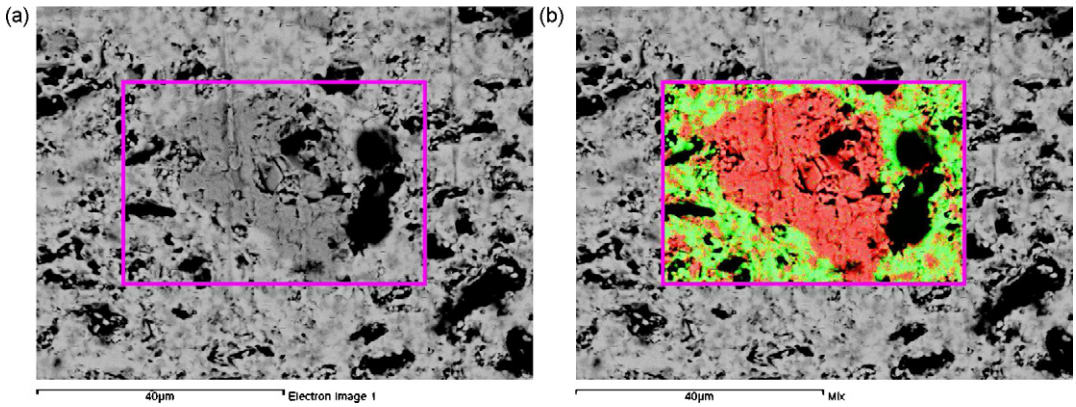

Fig. 6. (a) SEM-BSE image of selected region for EDS mapping; (b) EDS element mapping of selected region (red: Ni, green: Zr). (For interpretation of the references to color in this figure legend, the reader is referred to the web version of the article.)

For each image, we calculated the distribution of the pores radius (Fig. 7).

The same results but concerning the Ni-phase is reported in Fig. 8.

It is worth to point out that the Ni grain size distribution refers to Ni still being an oxide, since we proposed an image of a never-operated cell. We will show later how the Ni-phase agglomerates in an operated cell spreading the actual distribution towards higher equivalent radii.

To complete our first discussion on the granulometry distribution of the phases of a composite electrode we present a summary of the average distribution of the "Ni", "Zr" and "Pores" phases for the five image objects of our demonstrative analysis (Fig. 9).

The mean grain size for each phase is estimated by the software upon the granulometry distribution presented above. These are relevant values since they will be used for electrodes microscopic models presented in the next sections. It is worth to note that the plotted granulometry distributions have some resemblance to the gamma or prime beta distributions family. This is a kind of family of probability distributions defined by two parameters, respectively, a shape and a scale parameter. These probability distributions have several interesting features from a mathematical point of view. To give an example, one of the properties is that the statistical mean equals the algebraic product of the two above-mentioned parameters. This feature could be used to reduce the image data necessary to have a statistically good estimate of the grain size of each binarized phase, being the latter the mean of the each granulometry distribution. In Table 2 are reported the values of porosity, volume fraction of each phase, mean grain size and thickness of the anode electrode analyzed in this section through image analysis. In this same table are reported the results of cathode double layer, studied in Section 3.3.

Once the binarized images for each phase of a composite electrode are available, in our case a SOFC anode support, we can perform zero and first order statistics operations in order to extract quantitative information in 2D binary images (phase fraction, grain size, particles and pore distribution) and to describe the topology of each phase. The term topology indicates the spatial connectivity relations between the image objects. This is possible since the acquired digital images are considered as a stochastic and random

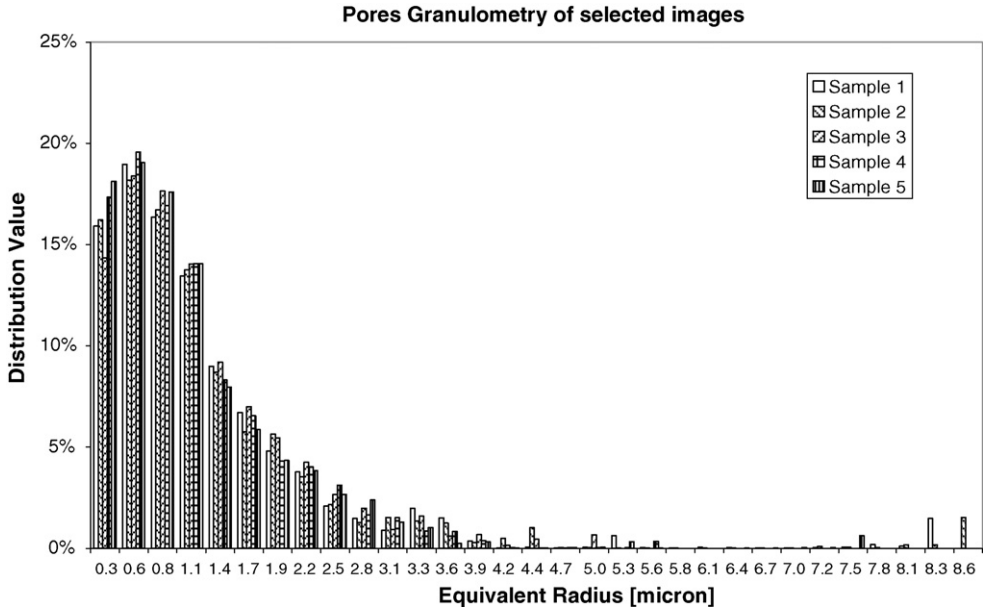

Fig. 7. Comparison of pores distribution from five samples of ASC1 anode support.

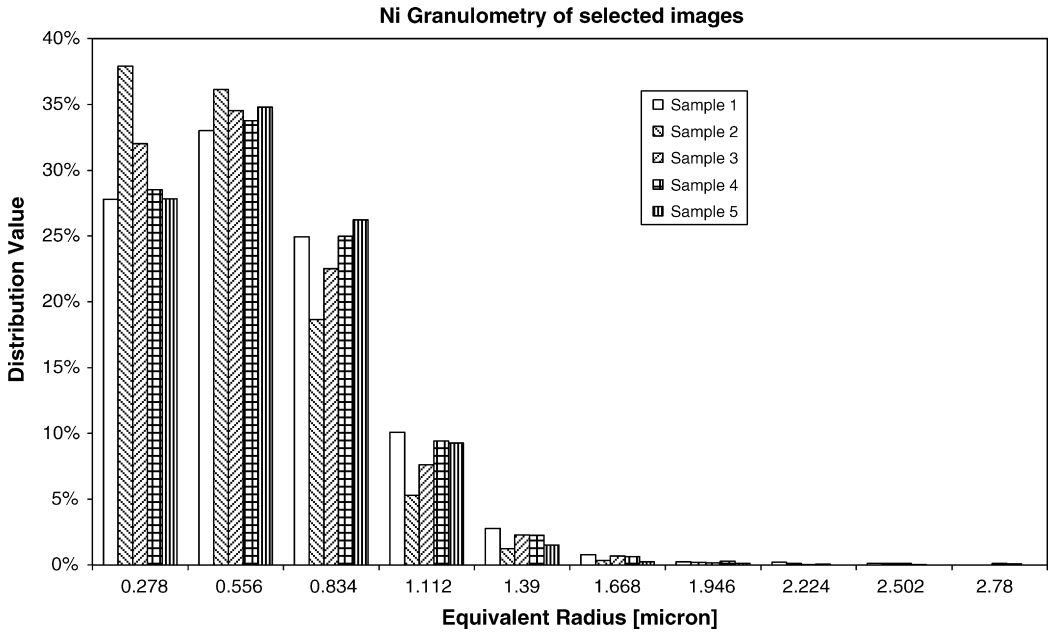

Fig. 8. Comparison of Ni distribution from five samples of ASC1 anode support.

Table 2
Microstructural characterization of ASC1 composite electrodes.

Image analysis—microstructural results						
Image type	Porosity [%]	Vol. electronic phase[a] [%]	Vol. ionic phase[b] [%]	Grain size electronic ph.[a] [μm]	Grain size ionic ph.[b] [μm]	Thickness [μm]
ASC1 SEM-BSE/anode support (Fig. 4)	26	45	29	0.5	0.8	520
ASC1 SEM/anode support (Fig. 1)	25	44	31	0.5	0.8	14
ASC1 SEM-BSE/cathode active layer (Fig. 16)	7	48	45	0.5	0.6	–
ASC1 SEM-BSE/cathode collector layer (Fig. 16)	30	70	0	1	0.8	18
Operated ASC1—optical (Fig. 13)	32	34	34	1	–	–

[a] Ni for the anode electrode and LSM for the cathode layers.
[b] YSZ for both electrodes.

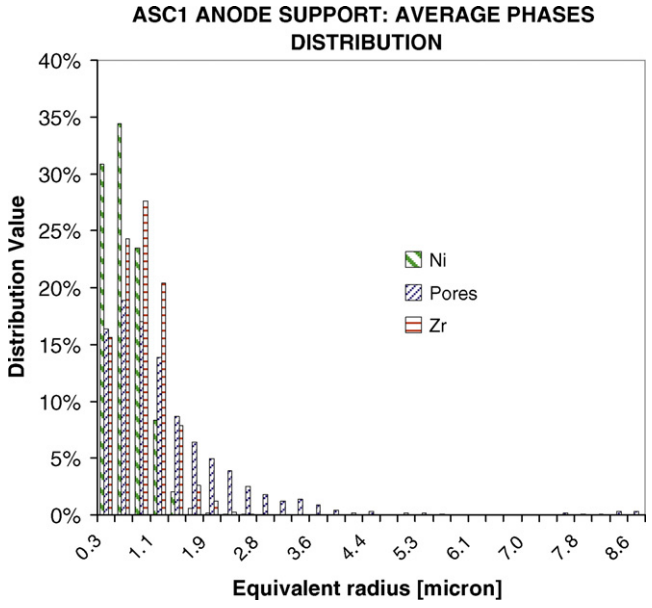

Fig. 9. Average phase distributions for an ASC1 anode support.

process. This allows one to simplify the analysis of image properties and characteristics. Then, in a binary image we can define the so-called phase functions which are associated to each phase constituting the image:

$$Z_{\Gamma}(\mathbf{x}) = \begin{cases} 1, & \text{if } \mathbf{x} \text{ belongs to phase } \Gamma \\ 0, & \text{if not} \end{cases}, \quad (1)$$

where $\mathbf{x} = (i, j)$ represents a position vector with regards to a reference origin, and Γ can be either one phase or another. It is presumed, a priori, that the microstructure representative images have statistical homogeneity.

Since we consider the images as stochastic processes, we can describe their properties by mathematically defined statistical quantities. In particular, we consider proper integrals of the phase functions designed to capture both global and detailed geometric information about the image. Clearly the application of the integral operator allows one to get rid of most of the unessential details, with the exception of those which are useful to characterize the image as a whole. For example, if we consider a given pixel (i.e. elementary discretization) in an image, by observing the chance of this pixel belonging to a pore, a one-point statistics is recovered. The same concept can be obtained by integrating the corresponding phase function and normalizing the result. For this reason, from a statistical point of view, the volume fraction of a solid phase of a composite structure or its porosity (being the pores just another phase of the structure) is a proper integral of the corresponding

phase function. Going deeper in our examination by observing the chance of two random pixels belonging to a pore, we can define a two-point autocorrelation function, and so on for defining multiple-point autocorrelation functions.

For a SOFC electrode we can describe each phase by the porosity as:

$$\phi_\Gamma = \left\langle Z_\Gamma(\mathbf{x}) \right\rangle, \tag{2}$$

where the operator $\langle\rangle$ represents the normalized spatial integral over the domain defined by the considered image.

For stochastic processes a correlation function is the correlation between random variables at two different points in space or time. If one considers the correlation function between random variables at the same point but at two different times then one refers to this as the autocorrelation function.

For image analysis purposes, the two-point autocorrelation function is then defined as (see Adler et al. [23]):

$$R_Z(u) = \frac{\left\langle [Z_\Gamma(\boldsymbol{x}) - \phi_\Gamma]\,[Z_\Gamma(\boldsymbol{x}+\boldsymbol{u}) - \phi_\Gamma] \right\rangle}{\phi_\Gamma - \phi_\Gamma^2}, \tag{3}$$

for each random dislocation in the image plane. Furthermore, with the hypothesis of an isotropic medium, the correlation depends only on $u = |\mathbf{u}|$, which represents a spatial dislocation in the image plane. Regarding its practical meaning, the autocorrelation function gives us the probability of two pixels separated by the distance u of belonging to the same phase Γ.

With the hypothesis of a statistically homogeneous electrode, the autocorrelation function for each phase Γ, mathematically defined by Eq. (2), can be practically calculated on the binarized images replacing the denominator of the second term in Eq. (3) by the following term, called simply correlation function:

$$\begin{aligned} C_\Gamma(u) &= \left\langle Z_\Gamma(\boldsymbol{x}) Z_\Gamma(\boldsymbol{x}+\boldsymbol{u}) \right\rangle \\ C_\Gamma(u) &= \left\langle Z_\Gamma(i,j) Z(i+u,j) \right\rangle \end{aligned}, \tag{4}$$

being i and j the coordinates of a generic pixel on the image plane.

The latter expressions are derived considering that for each phase the binarized image S is divided into two sub-sets, namely say S_1 and S_2, being $S = S_1 \cup S_2$ and $S = S_1 \cap S_2 = \varnothing$; in order to calculate $C_\Gamma(u)$, S_1 is translated by a distance u along the i-axis; it yields $S_1(+u)$. The spatial average indicated in Eq. (4) is then replaced by an intersection of images:

$$\left\langle Z(i,j) Z(i+u,j) \right\rangle = S_1(+u) \cap S. \tag{5}$$

Then for calculating the expression in Eq. (2), the denominator term is evaluated just as presented, while the other operations are simply algebraically performed.

If the dislocation is not just along a single axis, but in multiple directions, we could write a more general form of Eq. (4), which could be:

$$C_\Gamma(u,v) = \left\langle Z_\Gamma(i,j) Z_\Gamma(i+u,j+v) \right\rangle. \tag{6}$$

The commercial code allows one to determine the autocorrelation function for the binarized images. The default method is the spatial method, which considers dislocation of the image in one direction only (Eq. (5)). This method can present large fluctuations, even though this is not the case for the binary images analyzed in this paper. Anyway, in case of large fluctuations, it is possible to consider the frequential method, which is basically equivalent to consider all the possible dislocations in all directions. In practice, the result obtained is equivalent to determining the spatial autocorrelation function in all directions (at 360°).

For the sake of example, the correlation function of nickel binarized phase, obtained by the spatial method with only one direction considered, is presented in Fig. 10.

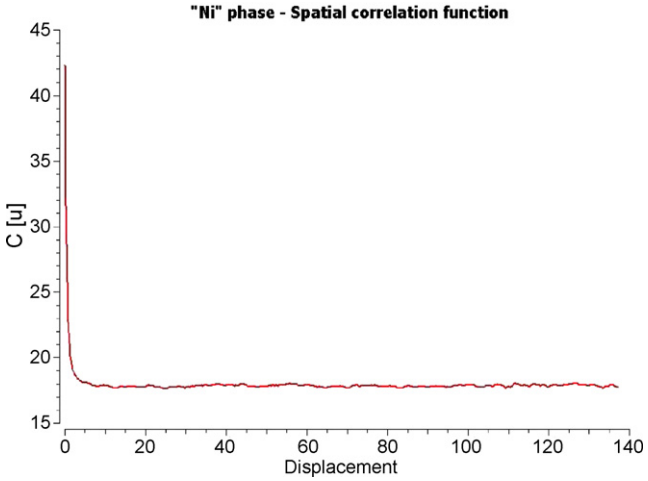

Fig. 10. "Ni" phase spatial-correlation function.

From the spatial-correlation function is possible through the commercial software to reconstruct in 3D the phase structure. The method used is the Truncated-Gaussian method. This method is described by Adler et al. [23] and its fundamental hypothesis states that a porous microstructure can be fully described by the one-point and two-point statistics of its phase function. It also considers that the porous microstructures are statistically homogeneous and isotropic. The porous media is constructed in a discrete manner; it is composed of N_c^3 small elementary cubes, each having size w, which corresponds to the pixel of the analyzed image. These elementary cubes correspond either to pore or solid phase. The structure is then generated filling a certain volume with these elementary cubes, each of one either belonging or not to the phase selected to be reconstructed, and being given the phase porosity and autocorrelation function. Basically the use of the Truncated-Gaussian method consists in the generation of a random space function $Z(\mathbf{x})$, which is equal to 0 in the solid phase, and 1 in the pore phase. As already stated, the random generation of the structure takes place having as constraints the average statistical quantities described before, i.e. the porosity ϕ and the autocorrelation function $R_Z(\mathbf{x})$, and the fact that the generated 3D structure has a finite size $w \cdot N_c$ (being this product the cube length L_c). A more detailed description on how the method for 3D reconstruction is presented in Appendix A.

Next we present some representative 3D structure image output obtained with the commercial code using the Truncated-Gaussian method (Figs. 11 and 12). The sources for reconstructing the 3D structures are the binarized 2D phase images along with the calculated spatial-correlation function.

These 3D structures can be used in a Lattice Boltzmann Method (LBM) code to compute the diffusion of reactants gases to the anode electrode, evaluating specific fluid-dynamic quantities, such as tortuosity [11,22]. The reconstruction of the Ni-phase could be used, instead, for computing the flow of the electronic charge. Actually, the commercial software allows one to reconstruct just a phase at once, according to the mathematic method described before. The limit lays in the Truncated-Gaussian method, which considers just a medium with two phases. For this reason, it is not currently possible using this method to have a simultaneous reconstruction of each phase of a SOFC composite electrode, which has three phases (two solid and one void, the pore phase). Actually we can reconstruct one phase at once considering the other two phases as the background. So it is possible to obtain the 3D reconstruction of the whole structure. The problem is then putting together the tree reconstructions in the same volume space, preserving the correlation function of

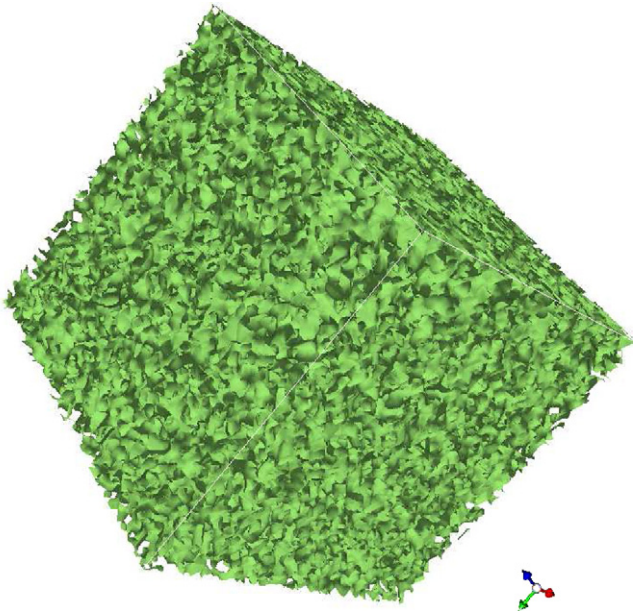

Fig. 11. Ni-phase 3D reconstruction (cube 27.8 μm × 27.8 μm × 27.8 μm, resolution 3.6 pixels μm^{-1}).

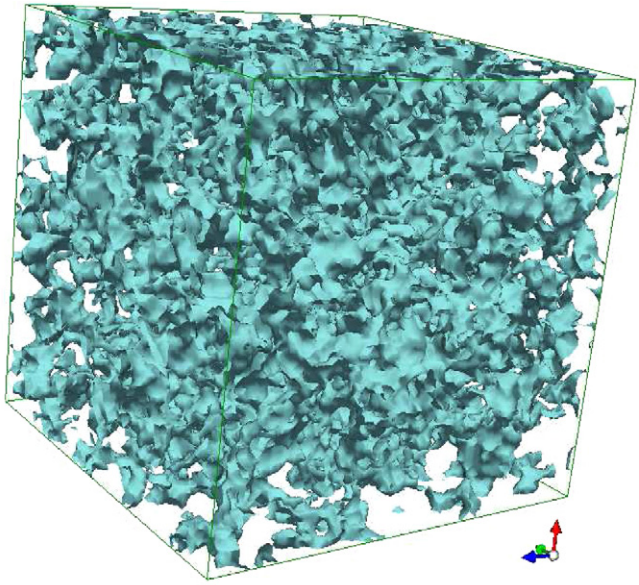

Fig. 12. Pores phase 3D reconstruction (cube 27.8 μm × 27.8 μm × 27.8 μm, resolution 3.6 pixels μm^{-1}).

each phase created separately. This a limitation if one would evaluate for example the three-phase boundaries (TPB) of the electrode, which requires having a volume, filled simultaneously with the all three phases.

3.2.1. Nickel agglomeration

The coarsening of nickel in an anode composite structure is a phenomenon well described in [29–33]. As far as the Ni/YSZ cermet anodes are concerned, the most predominant microstruc-

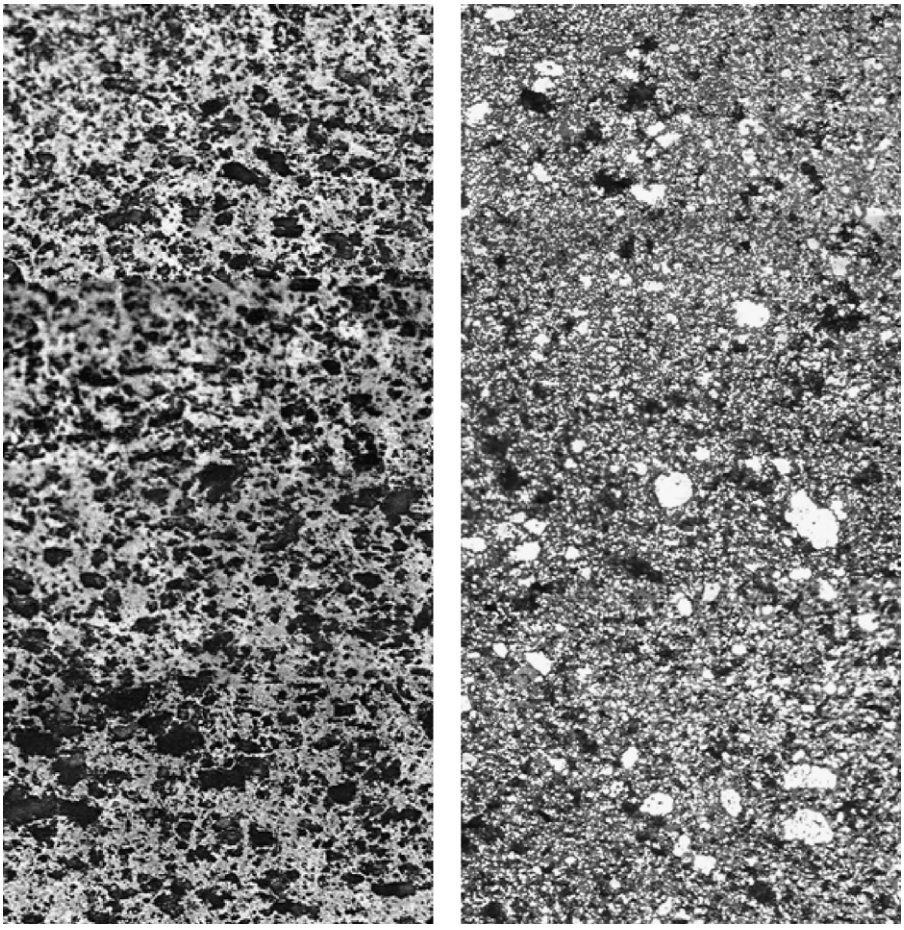

Fig. 13. Cross-section of an ASC1 anode support before (left) and after testing (right).

ture change is the agglomeration and coarsening of Ni-phase. The phenomenon has been investigated from a microscopic point of view through image analysis techniques revealing an increase of the mean particle size of Ni particles. The main reason for the agglomeration of Ni in the Ni/YSZ system is probably due to the poor wettability between the metallic Ni and YSZ oxide phase. Nikolopoulos et al. [29,30] studied the wettability and interface reaction between Ni and YSZ system in the temperature range of 1250–1500 °C and purified Ar/4%H_2 atmosphere. Molten Ni showed no wettability towards YSZ ceramic phase ($\theta = 117°$). Additives such as Ti, Cr, Mn and Pd have certain effect on the wettability between Ni and YSZ. However, the effect on the interfacial energy of the Ni/YSZ system appears to be small. Due to low melting temperature, pure Ni has a high tendency to sinter at SOFC operation temperatures (e.g. 1000 °C). The sintering of pure Ni anodes in reducing environment is very rapid, leading to the formation of isolated islands. Therefore, the prevention or reduction of agglomeration and sintering of metallic Ni-phase in the Ni/YSZ cermet electrodes rely heavily on the microstructure optimization of the Ni/YSZ cermets.

In Fig. 13, is shown the cross-section of an ASC1 cell before and after testing.

Seeing the Ni structure agglomerated in some regions of a brand new cell, means that Ni has formed these agglomerates during the anode sintering (last step of the component manufacturing). However, as shown later in this paper, this phenomenon takes also considerably place during the cell operation life. In order to show that, we compared the Ni-phase distribution in a brand new cell with that in an operated cell (as shown in Fig. 13) of the same type. What we suspected to be Ni agglomerates were confirmed by the EDS analysis. If we assume that the brighter phase is Ni, it is important to note how the Ni-phase tends to form some large agglomerated, even if homogeneously distributed over the anode section. In order to clarify this phenomenon, we evaluated the distribution of the Ni-phase in a cell brand new and operated (Fig. 14).

It is really interesting to report the large nickel agglomeration that was occurred in the cell after a short operational life (about 300 h). Very large "islands" of Ni are present. In the next section we try to evaluate the impact of this degradation phenomenon on the cell electrical behaviour using the percolation theory.

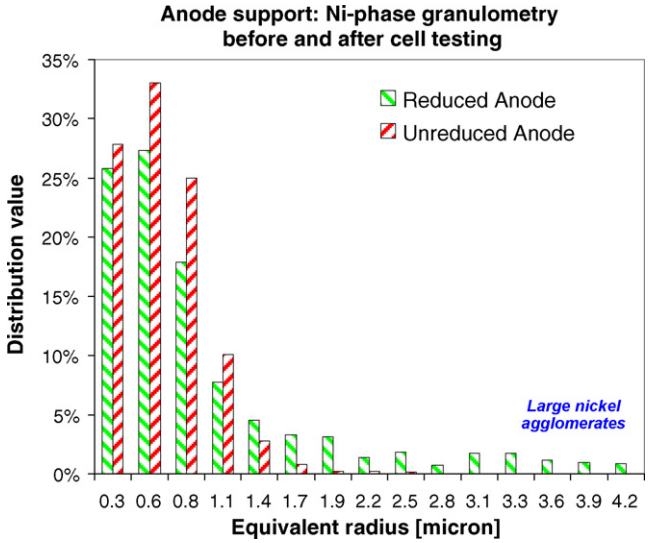

Fig. 14. Comparison of Ni-phase granulometry in an ASC1 cell before and after testing.

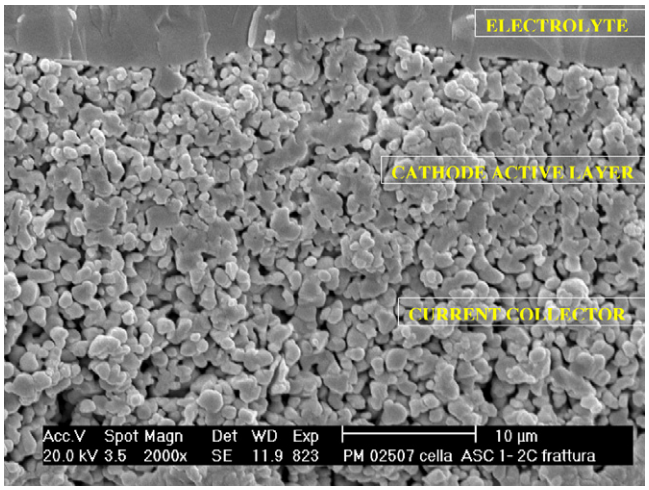

Fig. 15. SEM image of the ASC1 cell (from top to bottom: 8YSZ dense electrolyte, LSM/8YSZ active layer, LSM porous current collector layer).

3.3. Microscopic properties of cathode

The study of the microstructure of cathodic double layer is somewhat more difficult compared to that of the anode layer. This is due to its materials composition, to its much finer microstructure and the reduced thickness of the layers. In Figs. 15 and 16 we present the cross-sections images of the double-layer cathode we utilized for the image analysis. By means of EDS microscopy, it was hard to distinguish the ionic phase (YSZ) from the electronic one (LSM). The two phases appear to have a similar grain structure and they are also highly mixed together. By using SEM-BSE detector finally we succeeded in determine the fraction volumes of YSZ and LSM.

In Figs. 17 and 18 we report the binarized distribution of each phase for the active layer, and the current collector layer (as done previously on the anode electrode). We estimated the porosity of the active layer and the current collector layer as well. Basically for the cathode electrode we repeated the same image analysis conducted on the anode.

Figs. 17 and 18 show quite well the different porosity between the cathode active layer and current collector layer. This is because the current collector layer mainly acts as a diffusion layer, letting the oxidant penetrate the active layer, where the electrochemical reaction effectively takes place. The reason why the latter layer is denser, lays on the fact that the composite solid phase made of

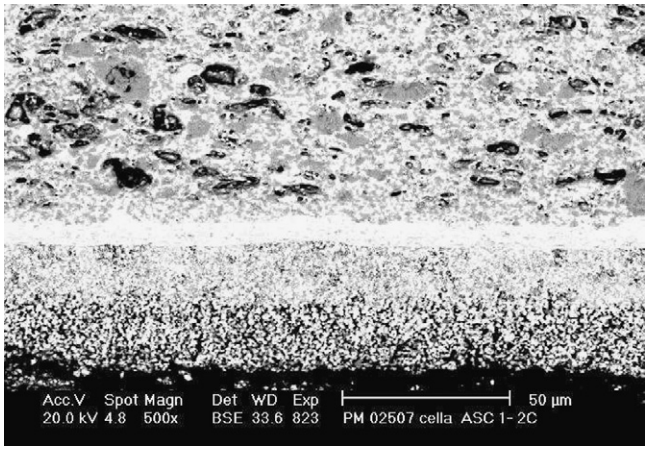

Fig. 16. SEM-BSE micrograph of the whole cell cross-section (from top to bottom: NiO/8YSZ anode support, 8YSZ dense electrolyte, LSM/8YSZ active layer, LSM porous current collector layer).

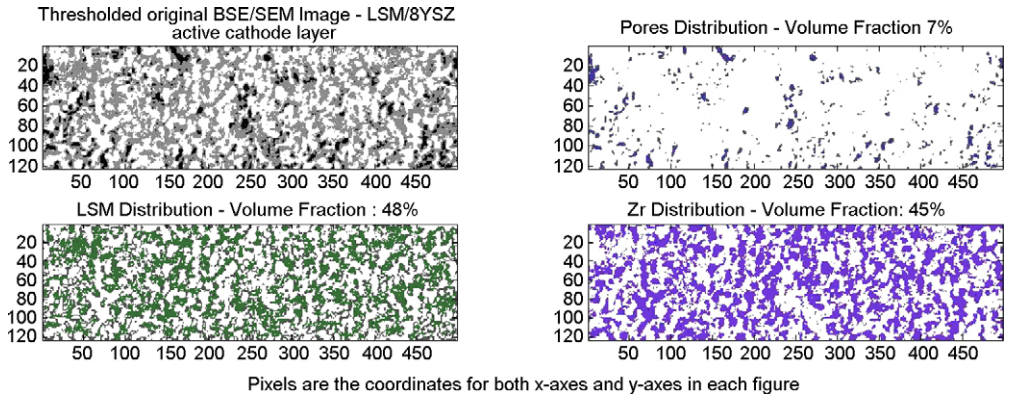

Fig. 17. Solid and pore phase distribution and volume fraction estimated through image analysis of the cathode active layer.

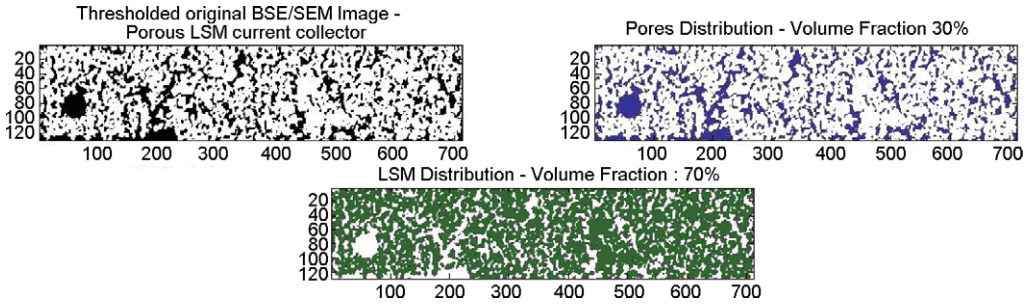

Fig. 18. Solid and pore phase distribution and volume fractions estimated through image analysis of the cathode current collector layer.

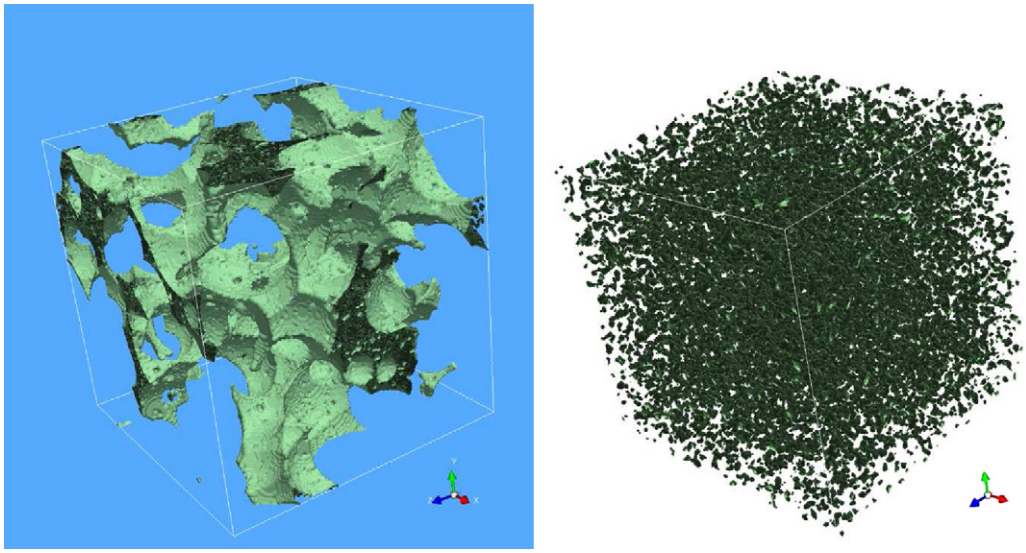

Fig. 19. (Right) 3D reconstruction of the porous cathode current collector layer (cube 20 μm × 20 μm × 20 μm); (left) close-up of the reconstructed structure.

LSM/8YSZ realizes a charge-transfer phenomenon instead of a mass transport phenomena.

We do not report again the correlation functions calculated for each binarized phase since we already showed this type of result for the anode, we just report as an example output of 3D structure of LSM porous current collector layer (Fig. 19).

4. Micro-models of composite electrodes

Image analysis is very powerful when its results can be used for modelling purposes. The high quality of information presented in this paper can be used in a multi-scale modelling approach starting from analytical microscopic models up to 3D electrical modelling of the electrodes and micro-fluidic modelling of the reactive species flowing through the pores.

In this section, the information obtained by the image analysis are used in order to estimate the cell design and its nominal operating temperature according to the investigated microstructure by using analytical models based on charge transfer and percolation theories [12,13,15,16,18,20,21].

4.1. Methodology of electrochemical analysis

The electrochemical characterization was performed by taking *V–I* measurements over a range of temperatures between 750 °C and 850 °C with hydrogen as fuel, and air as oxidant. Then polar-

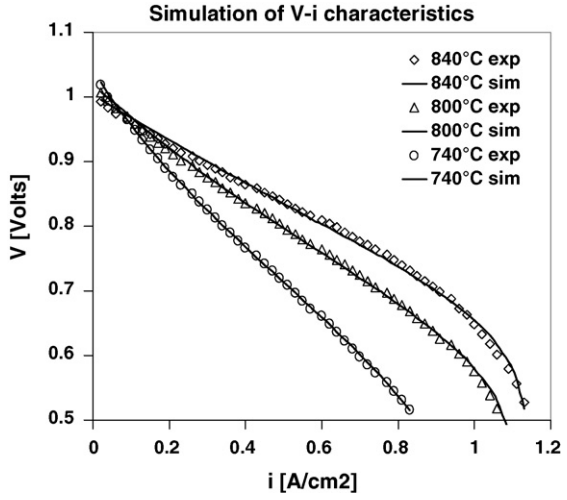

Fig. 20. Experimental and fitted by regression model polarization curves of anode-supported cell with LSM cathode.

ization curves were analyzed using a polarization model and by statistical regression on the experimental data. Parameter estimation method was used in order to break-down the main contribution of polarization resistance of the cell. Parameters such as effective exchange current density, ohmic resistance and anodic limiting current densities were obtained. The aim was to obtain macroscopic parameters describing the electrochemical performance and thus link them with the microscopic properties of the cell. Further details can be found in our previous work [25].

The cell voltage is expressed by Eq. (7):

$$V_c = V_{Nernst} - \frac{R \cdot T}{\alpha_{eff} \cdot F} a \sinh\left(\frac{i}{2 \cdot I_{o,eff}}\right) - R_\Omega \cdot i + \frac{R \cdot T}{2 \cdot F} \log\left(1 - \frac{i}{i_{as}}\right) + \frac{R \cdot T}{4 \cdot F} \log\left(1 - \frac{i}{i_{cs}}\right). \quad (7)$$

The Nernst potential, V_{Nernst}, was assumed equal to the measured open circuit voltage. The activation overvoltage was modelled using a single-term equation of the hyperbolic sine approximation of the Butler–Volmer equation. This is equal to assume one of the equilibrium exchange current densities sufficiently larger than the other, thus allowing the corresponding activation loss to be neglected [34]. The ohmic resistance in the model takes into account the resistance of electrolyte, electrodes, interface resistance and any contact resistance between current collectors. Concerning limitations in mass transport, it is expected that the anode is the critical electrode, so the anodic limiting current density is chosen to treat this losses and it is estimated through the fitting procedure; at the cathode a value of limiting current density is fixed.

The results of the fitting procedure are resumed in Fig. 20. Further details can be found in [25].

4.2. Relation between the cell's electrochemical performance and microstructure

In the latter section, the electrochemical analysis of the ASC1 cell combining current–voltage experiments and estimation of macroscopic parameters of a lumped polarization model was achieved. In particular the charge transfer limitations were modelled with the estimation of an effective exchange current density referring to the cathode electrode. An effective charge transfer resistance can be subsequently defined [12]:

$$\eta_{act} \cong \frac{R \cdot T}{z \cdot F \cdot I_{O,C}} \cdot i = R_{ct}^{eff} \cdot i. \quad (8)$$

The effective exchange current densities were 197 mA cm^{-2}, 112 mA cm^{-2} and 60 mA cm^{-2} at 840 °C, 800 °C and 740 °C, respectively. The following values can be then obtained for the effective charge transfer resistance: 0.12 Ω cm^2 at 840 °C, 0.21 Ω cm^2 at 800 °C and 0.36 Ω cm^2 at 740 °C, respectively. In order to evaluate the actual cell design in terms of charge transfer polarization, we used the latter values to calculate the intrinsic charge transfer resistance of the cathode electrode. For this purpose the equation developed by Tanner et al. (reported and described in [13]), has been used as well along with the actual cell microscopic values (summarized in Table 1); these values being extrapolated from the image analysis previously performed and electrochemical macro-parameters of the experimentally tested cell [25]. The estimated values of intrinsic charge transfer resistance were 2 Ω cm^2 at 840 °C, 3.6 Ω cm^2 at 800 °C and 6.2 Ω cm^2 at 740 °C. A first result is that the effective charge transfer resistance is decreased of more than one order of magnitude with the use of the composite layer [12,13].

In addition to the charge transfer resistance, the overvoltage related to the ohmic resistance has been estimated. In general the ohmic resistance is a sum of several contributes [35]: electrolyte, cathode functional layer (CFL), cathode current-collecting layer (CCCL), anode functional layer (AFL), anode current-collecting layer (ACCL) and resistances at interfaces and contact resistance. In terms of an equation this is expressed by:

$$R_\Omega = R_{8YSZ} + R_{LSM/8YSZ} + R_{LSM} + R_{Ni/YSZ} + R_{Ni/YSZ} + R_{contact} \ [\Omega\,\mathrm{cm}^2]. \quad (9)$$

In particular the following values of ohmic cell resistances were estimated: 0.135 at 840 °C, 0.189 at 800 °C and 0.322 at 740 °C [25].

Ohmic losses arise from the transport of ions and electrons in the ionic and electronic conducting phases of the composite electrodes and from the transport of ions in the electrolyte. The use of composite electrodes implies to spread the reaction zone over the whole 3D structure of the electrode, this means that the thickness of the electrode is a measure of the path of electrons from current collector to the reaction site and of ions, from the reaction site to the electrolyte in order to be transferred to the anode side. The transport of such charges is affected by several factors, in the following investigation it will be related to observed microscopic properties. Several authors [16,18,21] used particle coordination number in binary random packing of spheres and percolation theory in order to estimate the charge transport properties of composite electrodes. These properties basically include the estimation of effective electronic and ionic resistivities. Originally, the model was proposed by Bouvard and Lange [20] and it is based on physical meaningful equations, with reference to a mixture formed by matrix (m-particles) were inclusions are present. Using the equations derived by Bouvard et al., it was possible to estimate the effective charge transport properties of the cell's electrodes. The electrolyte ionic resistance was evaluated according to the following equations [36–38] and the experimentally observed thickness. The resistance of multi-layers electrodes was estimated with the use of microscopic observations of Section 3.3 and results proposed by the percolation theory. The ohmic conductivities relations of pure materials which were used in this analysis were assumed by [15]:

$$Ni: \sigma_{Ni} = 3.27 \times 10^4 - 10.653 \cdot T\,[\mathrm{S\,cm}^{-1}]; \quad (10)$$

$$8YSZ: \begin{cases} \sigma_{8YSZ} = (3.34 \times 10^2) \cdot e^{-10300/T}\,[\mathrm{S\,cm}^{-1}] \\ \sigma_{8YSZ} = 1/(0.00294 \cdot e^{10350/T_{cell}})\,[\mathrm{S\,cm}^{-1}] \end{cases}; \quad (11)$$

$$LSM: \sigma_{LSM} = (8.5 \times 10^2) \cdot e^{-1.28 \times 10^3/T}\,[\mathrm{S\,cm}^{-1}]. \quad (12)$$

Table 3
Contribution of each cell's layer to the total ohmic resistance.

Temperature [°C]	750	Contribution to total ohmic %	750	Contribution to total ohmic %	850	Contribution to total ohmic %
Ohmic total parameter estimation (ohm cm^2)	3.2E−01		1.9E−01		1.4E−01	
Electrolyte (ohm cm^2)	4.0E−02	12.5	2.3E−02	12.0	1.6E−02	11.9
Anode functional layer (ohm cm^2)	3.4E−02	10.7	1.9E−02	10.3	1.4E−02	10.1
Anode current-collecting layer (ohm cm^2)	7.5E−06	0.0	7.7E−06	0.0	7.8E−06	0.0
Cathode functional layer (ohm cm^2)	1.5E−01	45.5	8.3E−02	43.8	5.9E−02	43.3
Cathode current-collecting layer (ohm cm^2)	1.3E−05	0.0	1.2E−05	0.0	1.2E−05	0.0
Total arising from cell (ohm cm^2)	2.2E−01	68.7	1.2E−01	66.1	8.8E−02	65.4
Interfaces and contact resistance (ohm cm^2)	1.0E−01	31.3	6.4E−02	33.9	4.7E−02	34.6

In particular it was possible to determine some expressions of electronic and ionic resistivities for the different layers and for different microscopic assessments:

Anode (70% Ni, 30% YSZ; porosity: 20%; grain size Ni = 2.5 μm; grain size YSZ = 0.5 μm)

$$\begin{aligned}\rho_{e,eff} &= 3.07 \times 10^{-4} \cdot e^{-556.34/T}\,[\Omega\,\mathrm{cm}] \\ \rho_{ion,eff} &= 2.98 \times 10^{-2} \cdot e^{10350/T}\,[\Omega\,\mathrm{cm}]\end{aligned}. \quad (13)$$

Anode (50% Ni, 50% YSZ; porosity: 10%; grain size Ni = 0.5 μm; grain size YSZ = 0.5 μm)

$$\begin{aligned}\rho_{e,eff} &= 1.9 \times 10^{-4} \cdot e^{-556.61/T}\,[\Omega\,\mathrm{cm}] \\ \rho_{ion,eff} &= 7.1 \times 10^{-3} \cdot e^{10350/T}\,[\Omega\,\mathrm{cm}]\end{aligned}. \quad (14)$$

Cathode current-collecting layer (100% LSM; porosity: 30%)

$$\rho_{e,eff} = 1.7 \times 10^{-3} \cdot e^{1280/T}\,[\Omega\,\mathrm{cm}]. \quad (15)$$

Cathode functional layer (50% LSM, 50% YSZ; porosity: 20%; grain size LSM = 0.5 μm; grain size YSZ = 0.5 μm)

$$\begin{aligned}\rho_{e,eff} &= 3.2 \times 10^{-3} \cdot e^{1279.8/T}\,[\Omega\,\mathrm{cm}] \\ \rho_{ion,eff} &= 7.90 \times 10^{-3} \cdot e^{10350/T}\,[\Omega\,\mathrm{cm}]\end{aligned}. \quad (16)$$

In Table 3 it is shown the contribution of each layer to the total cell resistance. A critical layer in the correct cell design seems to be the cathode functional layer (CFL), in fact it affects the charge transfer resistance as well as the ohmic resistance; its contribution is around 45% of total ohmic resistance. The resistance at the interfaces and for contact with current collectors is derived for difference between the estimated value from parameter estimation and the total resistance evaluated through the use of the discussed microscopic model.

The polarization resistance of the cathode is plotted as a function of the thickness of the CFL in Fig. 21. This polarization resistance includes the charge transfer resistance as well as the electrode ohmic resistance. Increasing the thickness of the cathode functional layer, a decrease of polarization resistance is observed until reaching a minimum which is different for the investigated operating conditions. After this minimum, the polarization resistance increases as the contribution of the ohmic resistance of the layer increases. According to the simulation, the CFL, of 15 μm thickness, seems to be optimized for operating at around 850 °C. The optimization at lower temperature seems to be achieved with a thicker layer as shown from the curves, in particular at 750 °C the minimum is achieved for a CFL of 17 μm thick. As to be noted, that the reference actual design of the cathode active cell is a 17% value in porosity, a 0.7 μm mean grain size and a 14 μm in electrode thickness (data estimated from image analysis). Thus, the electrode seems to be optimized in the range of temperatures between 750 °C and 850 °C.

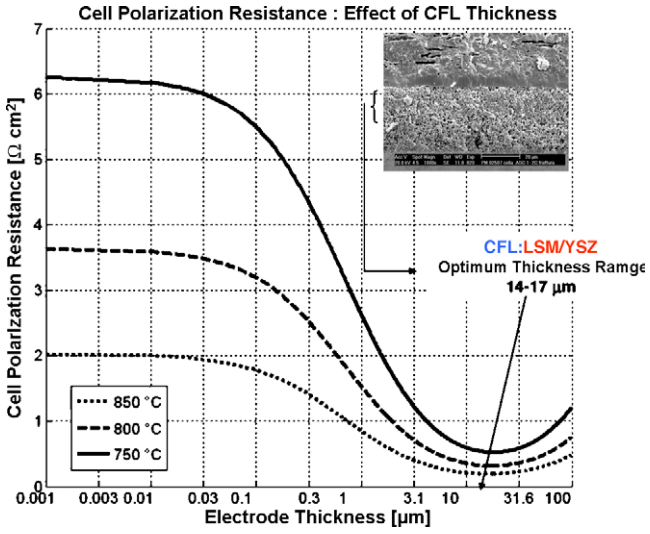

Fig. 21. Cathode polarization as a function of the CFL for different three operating temperatures.

5. Conclusions

The results presented in this paper show how we succeeded in coupling microstructural characteristics of the cell electrodes along with its electrical behaviour. The most innovative feature of this work is twofold: (1) using image analysis techniques for gathering important information of the electrodes microstructure and (2) putting together micro-models already developed for SOFC electrodes not just with microstructural data from literature, but with data taken directly from a real cell. Furthermore, for such an important parameter such as the cathodic resistance of charge transfer, namely R_{ct}, we proposed a way to extrapolate it from the cell electrical behaviour, again avoiding taking literature values as input for the adopted microscopic models. Finally, we used the models with these effective input data to provide a useful tool to check and predict the performances and the design of a commercial cell.

In this work we have also shown how image analysis represents a powerful method not only to analyze in details the microstructural properties of SOFC electrodes, but also to elaborate binary images which can be used to create 3D structure of the electrodes, conserving relevant statistical information of the electrode morphology and topology. The 3D reconstruction of SOFC composite electrodes is a valuable pre-processing procedure for the implementation of more realistic micro-models using an input geometry very close to the real one.

Acknowledgements

The authors would like to thank Mr. Battista Pernecco of "FN Nuove Tecnologie Servizi Avanzati SpA" and Dr. Andrea Ciampichetti and Mr. Massimo Agostini of "Centro Ricerche

Brasimone—ENEA" for providing the SEM images. A kind gratitude for his support goes to the ESSS—Engineering Simulation and Scientific Software Ltd., developer of the CHIMERA® software.

Appendix A. Truncated-Gaussian method for 3D reconstruction of electrodes' phases

Here it is described the algorithm that permits to reproduce 3D structures of composite electrodes, starting from the information extrapolated from the 2D images.

The method used for generating the discrete random variables, which verify Eqs. (2) and (3), is provided by Adler et al. [23] and Quiblier [28], and was further developed by Liang et al. [39].

Adler et al. [23] and Quiblier [28] showed that a random and discrete field can be devised from a non-correlated Gaussian field $X(\mathbf{x})$ when the latter one is successively passed through a linear and nonlinear filter. This can be realized in two steps starting from Gaussian and independent field called here $X(\mathbf{x})$. The random variables $X(i,j,k)$ of the starting Gaussian field are assumed to be normally distributed with mean equal to 0 and a variance equal to 1; these variables are also independent. Linear combinations of these variables by means of the coefficient field a yield a population $Y(\mathbf{x})$ which is still Gaussian but correlated; clearly the correlation depends upon the coefficient field of the linear combination. A linear operator can be defined by an set of coefficients $a(\mathbf{u}')$, where $\mathbf{u}'$ is the discrete displacement belonging to the discrete cube $[0,L_c]^3$. Outside this cube, the $a(\mathbf{u}')$ takes the zero value. A new random field $Y(\mathbf{x})$ which passes through a linear filter can be expressed as linear combination of the random variable $X(\mathbf{x})$ as follows:

$$Y(\boldsymbol{x}) = \sum_{\mathbf{u}' \in [0,L_c]^3} a(\mathbf{u}')X(\boldsymbol{x}_t), \tag{A1}$$

being the translated vector $\mathbf{x_t} = \mathbf{x} + \mathbf{u}'$. Periodic boundary conditions apply in order to deal with the finite cube N_c^3. It can be shown that the random variables $Y(\mathbf{x})$ are Gaussian and centered, under proper conditions [23]. The autocorrelation function $R_Y(\mathbf{u})$ of $Y(\mathbf{x})$ can be derived as [23]:

$$R_Y(u) = \sum_{r,s,t \in [0,L_c]^3} a(r,s,t)\,a(r+u,s,t), \tag{A2}$$

where $u+r$ and period boundary conditions apply again. The random variables $Y(i,j,k)$ have a standard normal distribution, though they are not statistically independent anymore. So the $Y(\mathbf{x})$ field is correlated, but it still not satisfactory since it takes its values in real number set, while the porous structure to be reconstructed has to be represented by a discrete-value function $Z(\mathbf{x})$.

Hence the population $Y(\mathbf{x})$ is transformed into a discrete population $Z(\mathbf{x})$ which takes only two values, 0 and 1, and the average value of is automatically set equal to the value of ϕ_Γ; this last transformation can be considered as a nonlinear filter. The random variables $X(i,j,k)$ are assumed to be normally distributed with a mean equal to zero and a variance equal to one and they are un-correlated. In order to extract $Z(\mathbf{x})$ form $Y(\mathbf{x})$, one applies a nonlinear filter G, which is a deterministic function of $Y(\mathbf{x})$ [23]:

$$Z = G(Y). \tag{A3}$$

Once G is known, the statistical properties of the random field $Z(\mathbf{x})$ can be derived from the properties of $Y(\mathbf{x})$. Since the random variable $Y(\mathbf{x})$ has a standard normal distribution, its distribution function $P(y)$ is given by

$$P(y) = \frac{1}{\sqrt{2\pi}} \int_\infty^y e^{-y/2} dy. \tag{A4}$$

The deterministic function G is defined in the following way. When the random variable Y is equal to y, Z takes the value z:

$$\begin{cases} z = 1 & \text{when } P(y) \le \phi_\Gamma \\ z = 0 & \text{otherwise} \end{cases}. \tag{A5}$$

In this way the average value of $Z(\mathbf{x})$ is equal to ϕ_Γ and its variance to $\phi_\Gamma - \phi_\Gamma^2$.

This procedure by Adler and Quiblier is analogous to solving an inverse problem, since it is necessary to determine the coefficients a and the correlation function $R_Y(u)$ before being able to reconstruct the porous structure. The mathematical determination of $R_Y(u)$ is described in details in Adler et al. [23], as well as for the determination of the a coefficients. The difficulty associated with the use of the linear filter presented above is to determine $a(\mathbf{u}')$ by solving Eq. (A2), which is a nonlinear system of equations. Generally solving this system of equations is time-consuming, difficult, and sometimes even not possible.

For these reasons Liang et al. in [39] showed how is possible to avoid the linear filter using Fourier transforms. They overcome this problem by the help of a mathematical theorem which enabled them to find an alternative way to generate the Gaussian field. Basically they generated the field $Y(\mathbf{x})$ from $X(\mathbf{x})$ using Fourier transform. From a computational point of view, then use of the fast Fourier transform algorithm, instead of laborious solution of nonlinear equations, represents a more preferable approach rather than using the linear filter method. The difference between the two methods is that with the Fourier transform $Y(\mathbf{x})$ is directly generated from its autocorrelation function $R_Y(u)$ and does not need the filter passing through $X(\boldsymbol{x}) \rightarrow Y(\boldsymbol{x})$.

This latter approach using Fourier transforms is the one used by the software CHIMERA® in the 3D reconstruction tool using the reconstruction method defined as the Truncated-Gaussian method.

References

[1] J. Malzbender, R.W. Steinbrech, J. Power Sources 173 (2007) 60–67.
[2] D.J.L. Brett, P. Aguiar, R. Clague, A.J. Marquis, S. Schottl, R. Simpson, N.P. Brandon, J. Power Sources 166 (2007) 112–119.
[3] J.R. Wilson, W. Kobsiriphat, R. Mendoza, H.Y. Chen, J.M. Hiller, D.J. Miller, K. Thornton, P.W. Voorhees, S.B. Adler, S.A. Barnett, Nat. Mater. 5 (2006) 541–544.
[4] E.D. Wachsman, Fundamental Mechanisms of SOFC Cathode Reactions, 7th SECA Workshop, 2006.
[5] E. Lara-Curzio, Durability and Reliability of SOFC Materials and Components Durability, 7th SECA Workshop, 2006.
[6] D. Bronin, Stack and Cell Performance Degradation: Causes, Effects and Solutions—the Current State of Knowledge, REAL SOFC Summer School, Varna, Bulgaria, September 2–7 (2007).
[7] D. Simwonis, F. Tietz, D. Stöver, Solid State Ionics 132 (2000) 241–251.
[8] K.R. Lee, S.H. Choi, J. Kim, H.W. Lee, J.H. Lee, J. Power Sources 140 (2005) 226–234.
[9] J.H. Lee, H. Moon, H.W. Lee, J. Kim, J.D. Kim, K.H. Yoon, Solid State Ionics 148 (2002) 15–26.
[10] K.R. Lee, Y.S. Pyob, B.S. Sob, S.M. Kimb, B.K. Lee, J.H. Hwang, J. Kima, J.H. Lee, H.W. Lee, J. Power Sources 158 (2006) 45–51.
[11] V.B. Kasula, L. Mercado, P. Asinari, M.R. von Spakovsky, Proceedings of IMECE 2007 ASME International Mechanical Engineering Congress and Exposition, Seattle, Washington, November 12–15, 2007.
[12] C.W. Tanner, K.-Z. Fung, A.V. Virkar, J. Electrochem. Soc. 144 (1) (1997) 21–30.
[13] A.V. Virkar, J. Chen, C.W. Tanner, J.W. Kim, Solid State Ionics 131 (2000) 189–198.
[14] T. Kenjo, S. Osawa, K. Fujikawa, J. Electrochem. Soc. 138 (2) (1991) 349–355.
[15] D.H. Jeon, J.H. Nam, C.J. Kim, J. Electrochem. Soc. 153 (2) (2006) A406–A417.
[16] J.H. Nam, D.H. Jeon, Electrochim. Acta 51 (2006) 3446–3460.
[17] P. Costamagna, P. Costa, V. Antonucci, Electrochim. Acta 43 (3–4) (1998) 375–394.
[18] P. Costamagna, M. Panizza, G. Cerisola, A. Barbucci, Electrochim. Acta 47 (2002) 1079–1089.
[19] A. Barbucci, P. Carpanese, G. Cerisola, M. Viviani, Solid State Ionics 176 (2005) 1753–1758.
[20] D. Bouvard, F.F. Lange, Acta Metall. Mater. 39 (1991) 3083.
[21] L.C.R. Scheineder, C.L. Martin, D. Bouvard, Y. Bultel, Proceedings of the Second European Fuel Cell Technology and Applications Conference, EFC2007, Rome, Italy, December 11–14, 2007.
[22] P. Asinari, M. Calì, M.R. von Spakovsky, B.V. Kasula, J. Power Sources 170 (July (20)) (2007) 359–375.

[23] P.M. Adler, C.G. Jacquin, J.A. Quiblier, Int. J. Multiphase Flow 16 (July–August (4)) (1990) 691–712.
[24] http://www.chimera4.com.br—CHIMERA 4.1 User Manual & Scientific Manual (2007).
[25] P. Leone, P. Asinari, M. Santarelli, R. Borchiellini, M. Calì, J. Power Sources 177 (2008) 111–122.
[26] V.A.C. Haanappel, M.J. Smith, J. Power Sources 171 (2007) 169–178.
[27] A. Lanzini, P. Leone, M. Santarelli, P. Asinari, M. Calì, R. Borchiellini, J. Fuel Cells Sci. Technol. 6, 011020 (2009).
[28] J.A. Quiblier, J. Colloid Interface Sci. 98 (March (1)) (1984) 84–102.
[29] P. Nikolopoulos, D. Sotiropoulou, J. Mater. Sci. Lett. 6 (1996) 1429.
[30] A. Tsoga, A. Naomidis, P. Nikolopoulos, Acta Mater. 44 (1996) 3679.
[31] S.P. Jiang, S.H. Chan, J. Mater. Sci. 39 (2004) 4405–4439.
[32] T. Iwata, J. Electrochem. Soc. 143 (1996) 1521–1525.
[33] S. Primdahl, M. Mogensen, J. Appl. Electrochem. 30 (2) (2000) 247–257.
[34] D.A. Noren, M.A. Hoffman, J. Power Sources 152 (2005) 175–181.
[35] F. Zhao, A.V. Virkar, J. Power Sources 141 (2005) 79–95.
[36] P. Costamagna, K. Honegger, J. Electrochem. Soc. 145 (11) (1998) 3995–4006.
[37] L. Baozhen, et al., US Patent No. 6,207,311 B1, Inventors Assigne: Siemens Westinghouse Power Corporation, 27/3/2001.
[38] N.F. Bessette, W.J. Wepfer, J. Winnick, J. Electrochem. Soc. 142 (1995) 3792–3800.
[39] Z.R. Liang, C.P. Fernandes, F.S. Magnani, P.C. Philippi, J. Petrol. Sci. Eng. 21 (1998) 273–283.